



Cerium–yttrium binary oxide microflower: synthesis, characterization and catalytic dehydration property

Cheng Pan, Ben-Hua Huang, Chao Fan, Xiao-Yong Li, Pei-Gen Su, A-Qun Zheng, Yang Sun*

Received: 17 May 2019/Revised: 3 July 2019/Accepted: 25 May 2020/Published online: 30 July 2020
© The Nonferrous Metals Society of China and Springer-Verlag GmbH Germany, part of Springer Nature 2020

Abstract Cerium dioxide has a comparatively lower $\text{Ce}^{4+}/\text{Ce}^{3+}$ redox pair, which leaves abundant oxygen vacancies on oxide lattice, also making incorporation of foreign ion and subsequent applications feasible and convenient. In this work, a series of cerium–yttrium mixed oxides were prepared by using polyvinylpyrrolidone as major template through sol–gel, which were further employed as catalyst for dehydration of aniline with formic acid into N-phenylformamide. Characterizations reveal that synthetic samples have a variety of morphologies including nanoparticle, microflower, and uniform microrods. The monitoring of particle size, zeta potential, and ultraviolet-visible (UV–Vis) of preparative solution indicate that self-assembly of polyvinylpyrrolidone and its subsequent reaction with metal ion determines sample morphology. In catalytic dehydration, all samples show high dehydration efficiencies that are comparable to those from anhydrous Na_2SO_4 and combination of dicyclohexylcarbodiimide with 4-dimethylaminopyridine and dichloromethane shows better outputs than water. In association with structural analysis, cerium looks more active than yttrium, while yttrium mainly plays as a structure-directing and pore-forming agent. This study may contribute to micro-/nanofabrication of rare earth composites and their catalytic applications.

Keywords Cerium–yttrium binary oxide; Microflower; Morphology; Formation monitoring; Catalytic dehydration

1 Introduction

The chemical property, synthesis and application of micro-/nanosized cerium dioxide (abbreviated as CeO_2 or ceria) have aroused extensive interests in recent years. First of all, the $\text{Ce}^{4+}/\text{Ce}^{3+}$ redox pair has an electrochemical potential of 1.3–1.8 eV, lower than many other redox pairs, indicating that cerium ion could be easily oxidized or reduced without degrading oxide framework [1], which would leave a lot of oxygen vacancies on oxide lattice, naturally facilitating some unique applications such as catalysis [2] and energy storage [3]. Secondly, micro-/nanosized CeO_2 usually shows much better stability than many other oxides with similar sizes, which is a critical parameter in promotion of particle activity for various applications [4]. At last, modulating oxygen vacancy of CeO_2 could be realized by doping of foreign metal ion into matrix lattice [4]. Overall, there is still a big room for exploring new CeO_2 materials through utilization of their unique properties.

Nowadays, CeO_2 has been shaped into different morphologies through various processes, such as hollow nanocubes stemming from a template-free method [5], hollow micro-/nanospheres from a solvothermal Ostwald ripening procedure [6] and nanoparticles from pulsed laser ablation in liquid [7], which all bring about updated or unexpected applications. On the other hand, functionalization of CeO_2 could be realized by oriented synthesis. For example, dispersion of cerium into α -aluminum oxide would not only confine size of CeO_2 nanoparticle within

Electronic supplementary material The online version of this article (<https://doi.org/10.1007/s12598-020-01475-5>) contains supplementary material, which is available to authorized users.

C. Pan, B.-H. Huang, C. Fan, X.-Y. Li, P.-G. Su, A.-Q. Zheng, Y. Sun*

Department of Applied Chemistry, School of Science, Xi'an Jiaotong University, Xi'an 710049, China
e-mail: sunyang79@mail.xjtu.edu.cn

3 nm, but also show much higher reactivity for oxidation of CO into CO₂ [8]. The hydrothermal treatment of Ce-based precursor with graphene oxide particle in liquid produces CeO₂/graphene oxide composite, exhibiting much higher activity than pure CeO₂ in photocatalytic degradation of methylene blue [9]. Obviously, there is a big space to develop new functional CeO₂, which may show unexpected catalytic performances.

The property, application and macro-/nanofabrication of yttrium oxide attract extensive attentions in recent years. Previously, yttrium oxide was used as sintering material for preparation of transparent ceramics [10], due to its high phase and thermal stabilities, along with low thermal expansion. As a rare earth element with certain alkalinity, yttrium oxide also shows great catalytic activities for a variety of reactions, including conversion of ethanol to propene and ethene [11], reduction of nitrogen oxide [12], and oxygen reduction and evolution of zinc–air batteries [13], all proposing a great prospect for developing yttrium oxide as catalyst.

On the other hand, there have been several efficient methods that can give various micro-/nanostructured morphologies to yttrium oxide. For example, the nanosheet could be obtained through solvothermal reaction [14], while nanoparticle appears over organosilane zeptoliter container [15]. Overall, use of template plays a key role in modeling yttrium oxide, also supposing optimization of template may bring about new morphology or structure.

According to the literature, polyvinylpyrrolidone (PVP) looks like a powerful stabilizer for producing metal-containing nanoparticle [16] or two-dimensional material [17]. It is supposed that PVP coordinates metal ion in solution, whose agglomeration limits size of metal-containing micelle into micro-/nanoscale, eventually leading to solid with proper morphology [18]. Furthermore, polyvinylpyrrolidone (PVP) contains both nitrogen and oxygen as coordinating atoms, making incorporation of multiple kinds of metal ions available, which would give binary or multicomponent metal oxide after aging or calcination. And meanwhile, PVP shows much higher solubility in both water and alcohol than in non-protic solvents [18], indicating that removal or precipitation of PVP template from synthetic composite has many options, which could protect other useful components that attached to PVP.

The dehydration reaction connects two molecules or reduces oxygen content of one individual molecule through releasing water, which has provided a lot of fine chemicals during the past years [19]. As one of the most useful and fundamental dehydrations in organic chemistry, amidation plays a key role in synthesis of pharmaceuticals and fine chemicals [20, 21], usually meaning addition of amine to an activated acyl compound like carboxylic acid,

anhydride, ester, or acyl chloride, releasing water or other small molecules simultaneously [22].

However, traditional amidation uses stoichiometric amount of coupling agents like p-toluenesulfonic acid or hydrochloric acid, often exhibiting low functional group tolerance, efficiency, selectivity, and product purification, and long reaction time, harsh condition, along with environmental burden [23], deserving more concerns and endeavors. Currently, some new methods are developed in order to make this process easier and cleaner, like utilization of boronic acid [24], n-butyl stannic acid [25], and polymer supported copper(II) complex [26] as catalyst, or employing ruthenium salt as catalyst, along with nitrile as nitrogen source [27], which all make progresses. However, in order to further overcome the above drawbacks, exploration of new solid catalysts appears to be a rational and powerful selection for this transformation.

In order to integrate structural and activity advantages of CeO₂ and yttrium oxide, this study would prepare cerium–yttrium binary oxide as catalyst for amidation. The PVP is used as a stabilizer for fabrication of micro-/nanosized catalyst, and molar ratio of cerium to yttrium in preparative solution is also adjusted to affect product morphology or activity. In the meantime, formation of metal oxide is also monitored by testing aqueous particle size, ζ (zeta) potential, and ultraviolet–visible (UV–Vis) spectroscopy of preparative sol. Generally speaking, this study may contribute to preparation of micro-/nanosized rare earth oxides, as well as to their applications for efficient and eco-friendly organic process.

2 Experimental

2.1 Materials

The cerium(III) nitrate hexahydrate (Ce(NO₃)₃·6H₂O, 99.5%), yttrium(III) nitrate hexahydrate (Y(NO₃)₃·6H₂O, 99.99%), polyvinylpyrrolidone (PVP, average molecular weight (M.W.) = 58,000), ammonium chloride (> 99%), and hexamethylenetetramine (HMT, 99.5%) were purchased from Adamas. The aniline (99.5%), formic acid (> 88.0%), dicyclohexylcarbodiimide (DCC, 99%), and 4-dimethylaminopyridine (DMAP, 99%) were purchased from Aladdin. Other inorganic salts and organic solvents were provided by local supplier, and distilled water is prepared in our laboratory.

2.2 Instruments

The scanning electron microscopy (SEM, JEOL JSM-6700F) using 20.0 kV in the absence of Au coating and transmission electron microscopy (TEM, JEOL JEM-

200CX) using 120 kV were used for microstructure measurements. The X-ray photoelectron spectroscopy (XPS, Kratos Axis Ultra DLD) employing monochromatic Al K α X-ray (1486.6 eV) as irradiation source was used for detecting sample compositions and chemicals state of elements, and the binding energy is calibrated by C 1s peak at 284.8 eV. The peaks were fitted by using Gaussian–Lorentz (G/L) product functions with 30% Lorentzian. The powdered low-angle ($2\theta = 0.5^\circ$ – 10°) and wide-angle ($2\theta = 10^\circ$ – 70°) X-ray diffractions (XRD) were collected on Philips X'Pert Pro diffractometer, employing Cu K α radiation ($\lambda = 0.15418$ nm) with interval of 0.05 ($^\circ$) \cdot s $^{-1}$.

The Brunauer–Emmett–Teller (BET) surface area, pore volume, pore radius, and pore size distribution were detected on Micromeritics ASAP 2020, employing N $_2$ adsorption isotherms at 77.35 K. Samples were degassed at 150 $^\circ$ C in vacuum before testing. Surface area was calculated by using multi-point BET method based on adsorption data with relative pressure (p/p_0) of 0.06–0.30. Total pore volume was obtained from N $_2$ adsorbed at $p/p_0 = 0.97$. Pore volume and pore radius were obtained by performing Barrett–Joyner–Halenda (BJH) method.

The Fourier transform infrared (FTIR) spectra were detected in KBr pellets on Bruker Tensor 27, having wave numbers of 400–4000 cm^{-1} . The thermo-gravimetric analysis (TGA) was performed on NETZSCH TG 209C featuring TASC 414/4 controller under nitrogen protection, with a heating rate of 10 $^\circ\text{C}\cdot\text{min}^{-1}$ at 35–800 $^\circ\text{C}$. The differential scanning calorimetry (DSC) was carried out on NETZSCH DSC 214 under nitrogen protection, with a heating rate of 10 $^\circ\text{C}\cdot\text{min}^{-1}$ at 50–300 $^\circ\text{C}$. The real-time monitoring of aqueous particle size and ζ (zeta) potential were run over Zetasizer Nano ZS90 spectrometer, Malvern. ultraviolet-visible (UV–Vis) spectroscopy was measured on UV 1800, Shimadzu.

The gas chromatography–mass spectrometer (GC–MS) was performed on GCMS-QP2010 Plus, Shimadzu, with Rxi-5 ms capillary column, whose length is 30 m and internal diameter was 0.25 mm. For GC part, column temperature was 60 $^\circ\text{C}$ and injection port temperature was 250 $^\circ\text{C}$, with sampling mode of split flow, split ratio of 26, and carrier gas of He. For MS part, ion source temperature was 200 $^\circ\text{C}$, while interface temperature was 250 $^\circ\text{C}$.

2.3 Synthesis of catalysts

As shown in Scheme 1, Ce(NO $_3$) $_3$ ·6H $_2$ O (C1, 4.50 mmol; C2, 3.00 mmol; C3 2.25 mmol; C4, 2.25 mmol; C5, 1.50 mmol; C6, 0 mmol), Y(NO $_3$) $_3$ ·6H $_2$ O (C1, 0 mmol; C2, 1.50 mmol; C3, 2.25 mmol; C4, 2.25 mmol; C5, 3.0 mmol; C6, 4.50 mmol), and HMT (C1, 0 mmol; C2, 5.00 mmol; C3, 5.00 mmol; C4, 0 mmol; C5, 5.00 mmol; C6, 0 mmol) were combined with a solution containing

ethanol (30 ml) and distilled water (15 ml) into a round-bottom flask (250 ml) under vigorous stirring. Then, NH $_4$ Cl (0.5 g, 9.3 mmol) was added, and resultant was further stirred at 20 $^\circ\text{C}$ for 3 h. The mixture was then aged in an autoclave at 180 $^\circ\text{C}$ for 24 h, and then the solid was filtered under reduced pressure, washed with distilled water (3 times, 5 ml) and absolute ethanol (3 times, 5 ml), dried at 60 $^\circ\text{C}$ in air. The products were obtained as gray-white powders, including C1 (0.11 g), C2 (0.54 g), C3 (0.65 g), C4 (0.58 g), C5 (0.66 g), and C6 (0.08 g).

2.4 Catalytic dehydration reaction

The aniline (2.0 mmol, 181 μl), formic acid (2.0 mmol, 76 μl), and catalyst (10 mol% Na over substrate for anhydrous Na $_2$ SO $_4$, 2 mol% DCC and catalytic amount of DMAP; 2 mol% Ce for C1–C5, 2 mol% Y for C6, according to XPS data, Table 1) were combined with CH $_2$ Cl $_2$ (or water, 10 ml) into a round-bottom flask (100 ml) under vigorous stirring. This mixture was further stirred at 20 or 80 $^\circ\text{C}$ for 6 h. The solid catalyst was separated by centrifugation. The filtrate was collected and tested on GC–MS for identification and quantification of catalytic product.

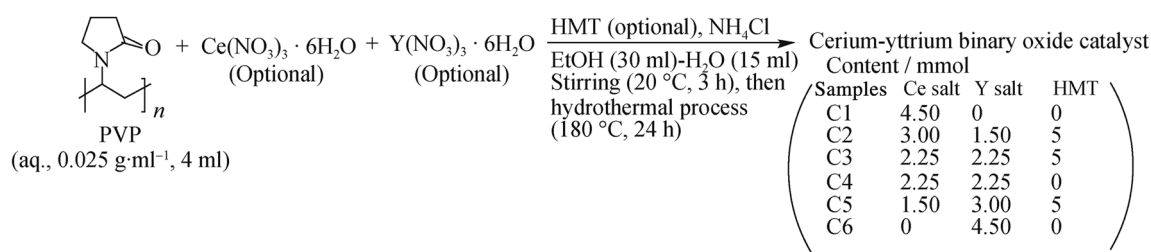
3 Results and discussion

3.1 Synthesis of binary oxide

As shown in Scheme 1, cerium and yttrium salts were combined with PVP into a water–ethanol mixed solvent, where PVP was used as template for stabilizing micro-/nanosized micelle, and optional addition of HMT may show influences on metal molar ratio of solid product, probably due to its coordination effect. On the other hand, the use of NH $_4$ Cl as additive may affect crystallization of oxide product [28]. Additionally, it seems interesting to observe whether modulation of metal ratio in preparative solution affects metal ratio of solid product (Scheme 1), which means a lot to catalyst design.

3.2 Morphology and internal framework

SEM provides a powerful method to detect morphology of solid sample, while TEM gives information on internal framework. At first, C1 is composed of uniform nanoparticles with sizes of 100–120 nm (Fig. 1a, b), probably indicating that PVP plays as a stabilizer in keeping nanosized appearance of solid sample (C1, Scheme 1). When yttrium begins to be doped into synthetic solution (C2, Scheme 1), the resulting sample turns out to be flower-like blocks consisting of fibers with length of 2–5 μm (Fig. 1c, d).



Scheme 1 Synthesis of cerium–yttrium binary oxides

Table 1 Binding energy and atomic composition of Ce, Y, C, N, and O on sample surface

Samples	Ce (3d)	Y (3p)	C (1s)	N (1s)	O (1s)	Ce(III)/% ^a	Ce/Y ^b
C1	881.8 (0.1) ^c	– ^d	284.8 (81.5)	–	531.8 (18.4)	24	–
C2	881.8 (0.7)	300.8 (1.8)	284.8 (78.6)	–	531.8 (18.9)	35	1/2.57 (2/1)
C3	882.8 (0.4)	301.8 (4.4)	284.8 (69.4)	397.8 (1.4)	531.8 (24.4)	21	1/11 (1/1)
C4	883.8 (1.5)	301.8 (0.2)	286.8 (75.6)	–	531.8 (22.7)	16	7.5/1 (1/1)
C5	884.8 (0.2)	301.8 (6.7)	284.8 (65.5)	394.8 (3.1)	531.8 (24.5)	14	1/33.5 (1/2)
C6	–	300.8 (7.3)	284.8 (63.0)	395.8 (5.8)	531.8 (23.6)	–	–

^aRelative content of Ce³⁺ = $A_{\text{Ce(III)}}/[A_{\text{Ce(III)}} + A_{\text{Ce(IV)}}]$, $A_{\text{Ce(III)}} = A_{\text{v}} + A_{\text{u}}'$, $A_{\text{Ce(IV)}} = A_{\text{v}} + A_{\text{v}}'' + A_{\text{v}}''' + A_{\text{u}} + A_{\text{u}}'' + A_{\text{u}}'''$, where A represents peak area (Fig. 3a–f) [29]

^bMolar ratio of metals on solid product, along with molar ratio of loading metals in sol–gel preparation in parenthesis

^cBinding energy (eV), along with elemental content (at%) in parenthesis

^dNot detected

When loading amount of yttrium equates to that of cerium in preparation (C3, Scheme 1), there are a lot of microflowers on SEM image, which are mainly composed of thin sheets with area of 0.5–1.5 μm^2 (Fig. 1e–h). From another point of view, the edge of C3 contains a lot of mesopores according to TEM observation (Fig. 2a–c), probably indicating that PVP acts not only as stabilizer, but also as pore-forming agent during preparation (C3, Scheme 1).

It is interesting to observe the effect of HMT on sample's morphology. In the absence of HMT (C4, Scheme 1), microflowers could still be found on SEM (Fig. 1j), but the edge of C4 looks flatter and denser than that of C3 (Fig. 2a–d). Herein, it is proposed that the presence of HMT may change sample composition, showing influences on morphology.

When loading amount of yttrium becomes two times as high as that of cerium (C5 vs. C3, Scheme 1), the microflower morphology is maintained according to SEM image (Fig. 1l–n), but petals look thicker (Fig. 1f, g, m, n). In the light of TEM, it appears that each petal of C5 is actually piled up with several very thin flakes (Fig. 2e, f). Therefore, loading more yttrium may not change the whole microflower appearance, but shows effects on fine structure of petals.

If yttrium salt is added as only metal precursor, the flower morphology disappears completely, and bunches of

microrods come into sight (Fig. 1o, p). In association with nanoparticle appearance of C1 (Fig. 1a, b), it seems that the microflower appearance represents formation of cerium–yttrium binary oxide under the present synthetic condition.

3.3 Chemical state of element

XPS appears to be an effective method to determine chemical state of element on synthetic sample. The binding energy and atomic composition are summarized in Table 1, while XPS survey scan is provided in Fig. S1 (Sect. 1, supplementary material). Firstly, C2 shows higher contents of cerium, yttrium and oxygen, along with lower content of carbon than C1 (Table 1). And meanwhile, C4 gives higher contents of cerium, yttrium, and oxygen, as well as lower content of carbon than C1 too (Table 1). Now that synthesis of C2 involves HMT, but blank for C1 and C4s (Scheme 1), it appears that loading of yttrium salt improves total metal content (cerium plus yttrium) on synthetic sample, but simultaneously excludes carbon, no matter whether HMT is used as additional ligand.

Furthermore, when loading of yttrium becomes equal to that of cerium in preparative solution (C3 vs. C2, Scheme 1), the resulting C3 shows higher contents of yttrium, nitrogen, and oxygen, together with lower contents

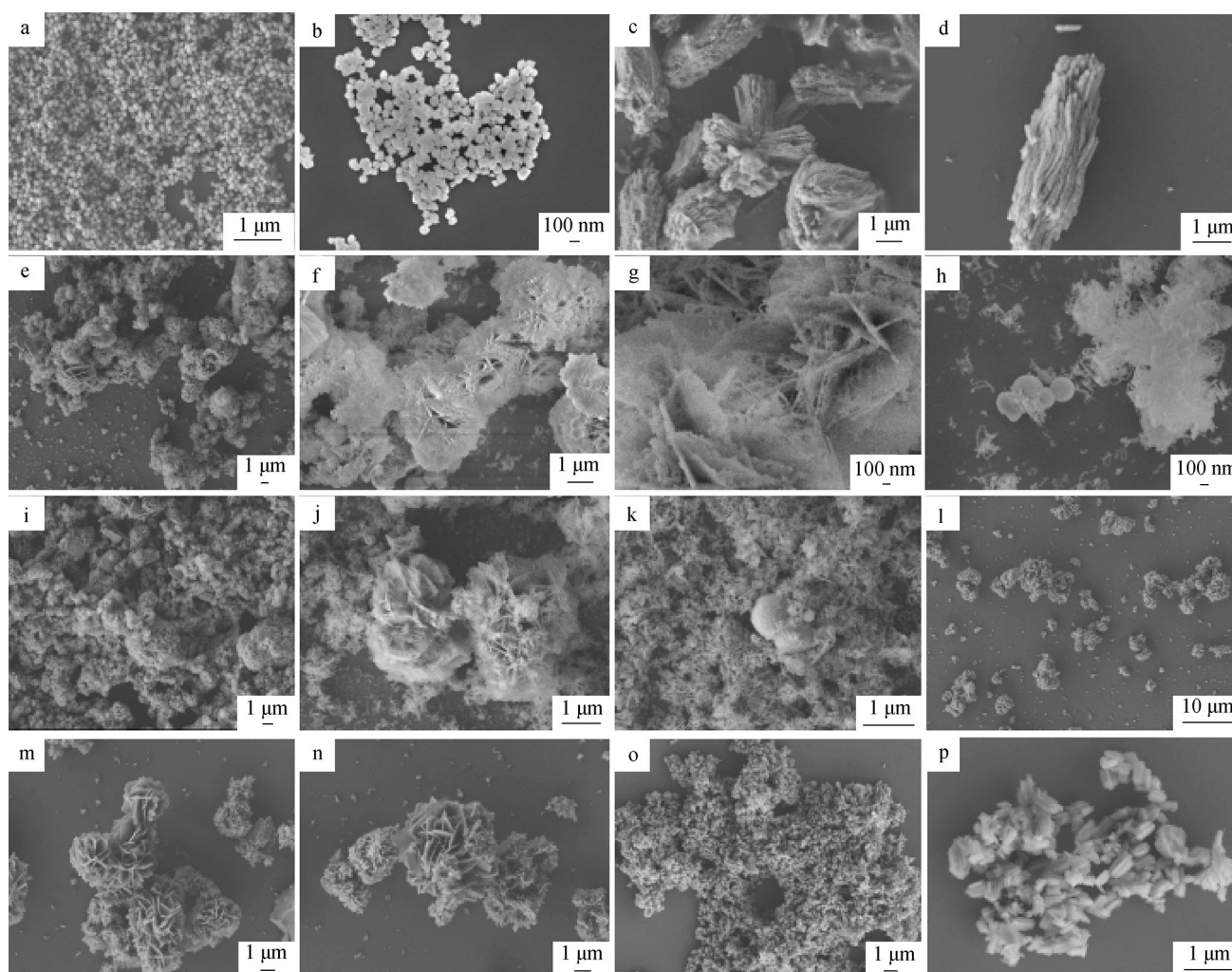


Fig. 1 SEM images of **a, b** C1, **c, d** C2, **e, f** C3, **g, h** C3, **i, j** C4, **k, l** C4, **m, n** C5 and **o, p** C6 samples

of cerium, carbon, and trivalent cerium than C2 (Table 1). If yttrium exceeds cerium in preparation (C5 vs. C3, Scheme 1), the solid contents of yttrium, nitrogen, and oxygen are also promoted, while cerium, carbon, and trivalent cerium are depressed accordingly (C5 vs. C3, Table 1). Moreover, C2, C3, and C5s show continuously elevated contents of total metal (Table 1). Therefore, when total metal content of preparative solution is fixed in the presence of HMT, increasing share of yttrium would improve yttrium content of solid sample together with incorporation efficiency of total metal, but decrease trivalent cerium content of total cerium.

It would arouse further interests to discuss the role of HMT in synthesis. C3 contains more yttrium, nitrogen, oxygen, and trivalent cerium, along with less cerium and carbon than C4 (Table 1). Then, total metal content of C3 is much higher than that of C4, and the molar ratio of Ce/Y is sharply conversed between C3 and C4s (Table 1). Thus, coordination of HMT may prefer yttrium to cerium in

preparative solution, which affects the composition of solid product.

It is also significant to discuss chemical states of metal, carbon, and oxygen on sample, which provides key information on catalyst structure. At first, Ce 3d regions of XPS of all relevant samples could be fitted into eight peaks, corresponding to four spin–orbit doublets, as shown in Fig. 3. Three of them labeled as $v-u$ ($3d_{5/2}-3d_{3/2}$), $v''-u''$ and $v'''-u'''$ could be ascribed to Ce^{4+} species, while the left one marked as $v'-u'$ is derived from Ce^{3+} components [29]. Therefore, all cerium-containing samples (C1–C5) cover both Ce^{4+} and Ce^{3+} contributions (Fig. 3a–e), but content of Ce^{3+} looks highly relevant to sample composition (Table 1).

Then, yttrium 3d regions of all samples are shown in Fig. 4. C2 shows binding energies of Y $3d_{5/2}$ and $3d_{3/2}$ photoelectrons at 156.7 and 158.3 eV, respectively, along with difference of 1.6 eV (Fig. 4a), characterizing Y^{3+} is fixed in phase of Y_2O_3 [30]. Another doublet appearing at

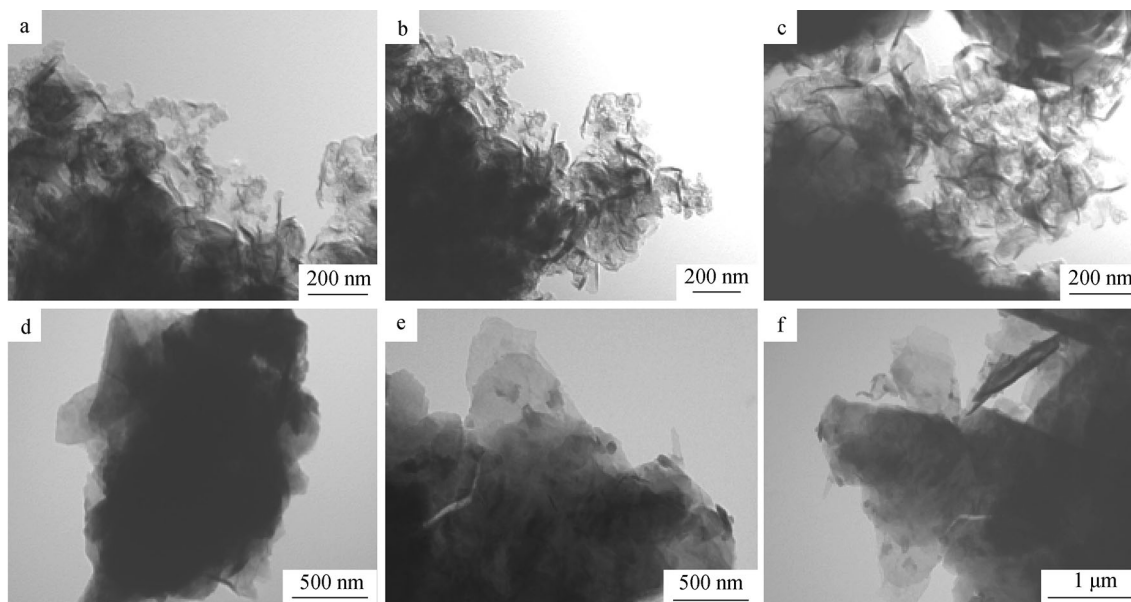


Fig. 2 TEM images of **a–c** C3, **d** C4, **e** C5, and **f** C5 samples

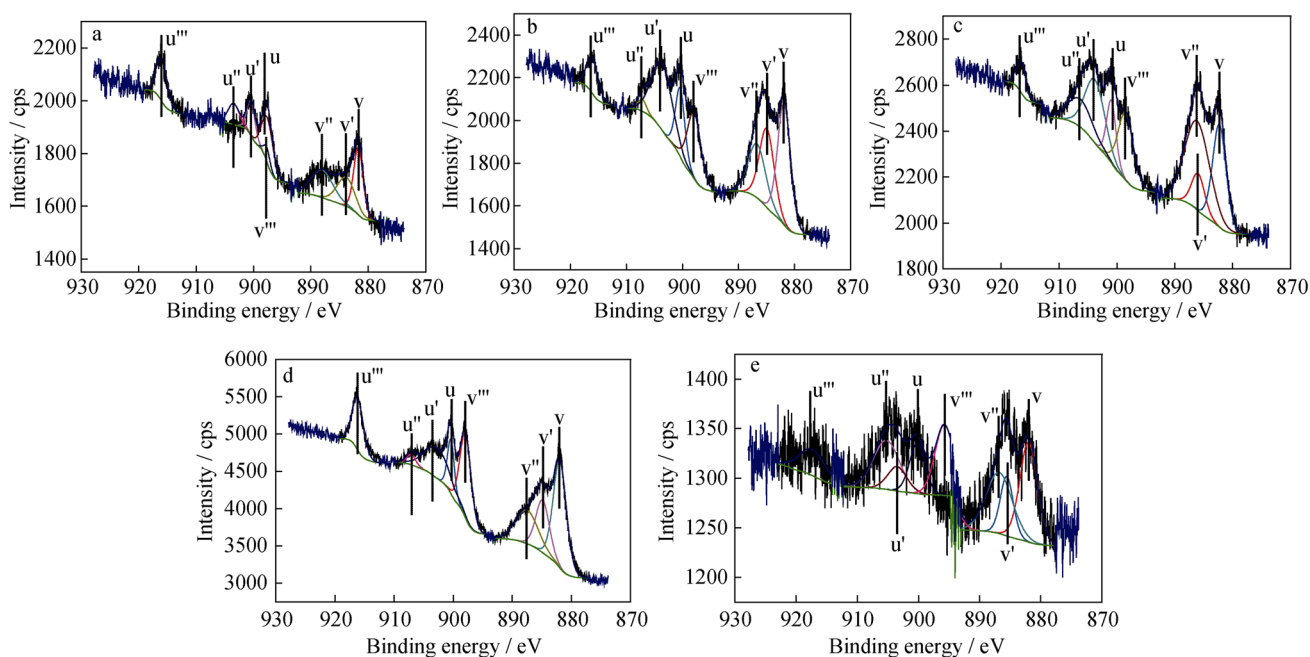


Fig. 3 XPS spectra of Ce 3d region for **a** C1, **b** C2, **c** C3, **d** C4, and **e** C5 samples

157.9 and 160.2 eV could be ascribed to Y^{3+} of cerium–yttrium mixed oxide phase (Fig. 4a). Herein, higher binding energies may stem from the newly generated mixed oxide lattice [31, 32]. The C3, C5, and C6 show similar yttrium 3d regions as C2 (Fig. 4a, b, d, e), indicating that the three samples all contain two kinds of yttrium components. Additionally, yttrium 3d core-level line of C4 seems difficult to fit, mainly due to the much lower yttrium content of C4 (Fig. 4c; Table 1).

Next, C 1s region of sample may provide information on structure of organic species. The peak occurring at 284.7 eV on C1 is representative of saturated hydrocarbons (sp^3 carbon), while the following two contributions at 286.0 and 288.7 eV could be assigned to carbonyl and carboxyl groups, respectively (Fig. S2, Sect. 2, supplementary material) [33]. On the other hand, when yttrium is loaded as only metal, the resulting C6 shows three C 1s peaks at 284.7, 285.1, and 288.7 eV, where the former two peaks

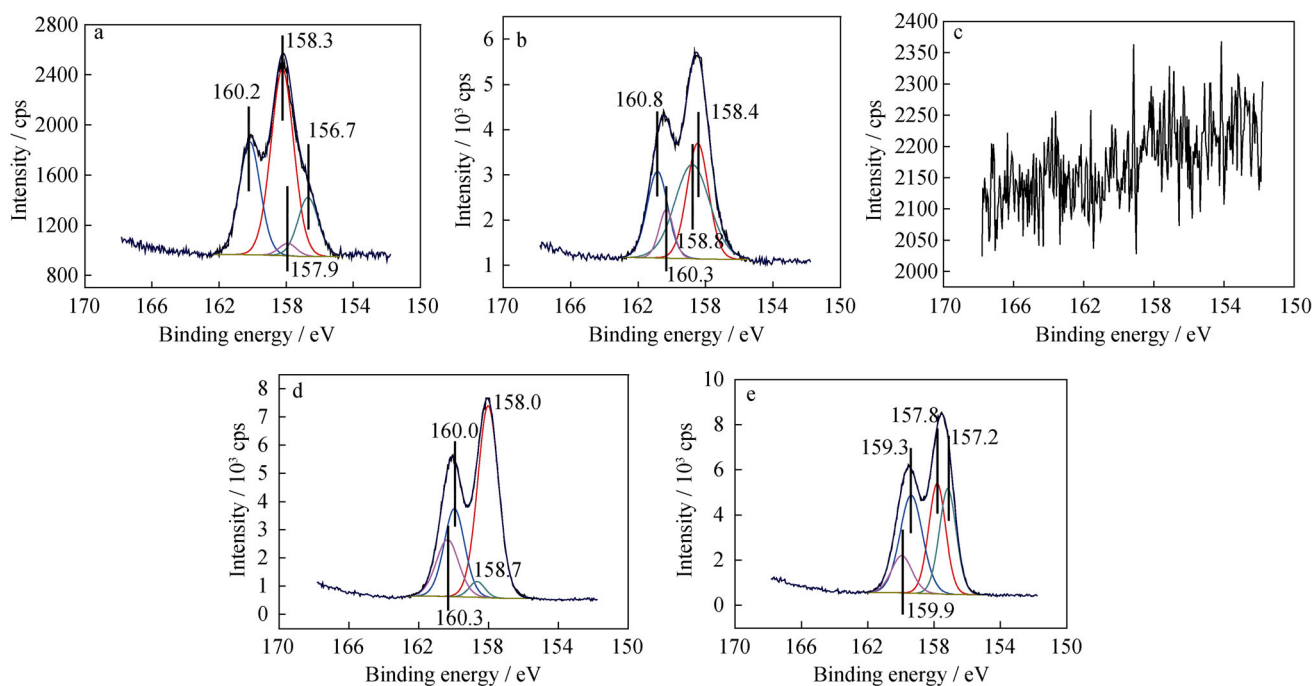


Fig. 4 XPS spectra of Y 3d region for **a** C2, **b** C3, **c** C4, **d** C5, and **e** C6 samples

may both indicate saturated hydrocarbons (sp^3 carbon), and the last one could be assigned to carboxyl group [33]. In the meantime, C4 shows a very similar C 1s core-level line as C6, where no carbonyl is detected (Fig. S2d, f).

However, the other three samples such as C2, C3, and C5s show a little different C 1s spectra with C1 and C6s, because the peaks at 289.7, 290.1, and 289.8 eV on C2, C3 and C5 are all indicative of the ester groups, which could not be found on spectra of C1 and C6 (Fig. S2a–c, e, f). Therefore, it can be seen that loading of HMT into preparative solution plays a key role in formation of ester group on organic species.

The O 1s region may provide structural information from another point of view. The C1 shows four contributions on O 1s region, where the first one at 528.8 eV seems to be oxygen of CeO_2 [34], the next at 531.0 eV is probably characteristic of oxygen of cerium salt, and the following two contributions at 531.8 and 533.2 eV could be assigned to oxygen of organic species (Fig. S3a, Sect. 3, supplementary material) [35]. There are four contributions on O 1s region of C3, where the first one at 529.6 eV looks like oxygen of yttrium oxide [31], the following one at 531.3 eV could still be ascribed to oxygen of cerium salt (Fig. S3c) [34]. The next one at 532.1 eV could be assigned to the oxygen originated from cerium–yttrium mixed oxide, probably because doping of cerium into yttrium oxide would increase the potential of oxygen compared with that from pure yttrium oxide [32]. The last oxygen contribution at 532.7 eV seems to be oxygen of organic species (Fig. S3c) [35].

The O 1s regions of C2 and C4s are quite similar. Herein, the contribution at 528.9 eV on spectrum of C2 could be ascribed to oxygen of cerium oxide (b, Fig. S3b), which could be also found on C4 (Fig. S3d) [34]. The two peaks at 531.6 and 531.8 eV on spectrum of C2 appear to be oxygens of cerium salt and cerium–yttrium mixed oxide (Fig. S3b), corresponding well to the components at 531.3 and 531.5 eV on spectrum of C4 (Fig. S3f). Therefore, C2 and C4 may have very close structures, particularly in terms of chemical composition.

C5 shows the first O 1s contribution at 531.1 eV, which is the highest among the former five samples (Fig. S3a–e), probably representing oxygen of pure yttrium oxide [31], because C5 has the lowest molar ratio of cerium to yttrium and may contain isolated yttrium oxide phase (Table 1). The following two peaks at 531.7 and 532.0 eV seem to be oxygens of cerium salt and cerium–yttrium mixed oxide (Fig. S3e).

In addition, when yttrium is loaded as only metal, there are three contributions on O 1s region of C6 (Fig. S3f). The first two peaks at 531.1 and 531.4 eV could be attributed to yttrium oxide and salt, respectively [31], while the following one with higher binding energy at 531.7 eV may be attributed to oxygen stemming from oxyanion or organic component (Fig. S3f) [35].

Based on XPS analysis, it can be seen that modulating composition of preparative solution would show important influences on composition of solid sample. The presence of HMT as active additive prefers incorporation of yttrium to

that of cerium, while its absence shows the contrary tendency.

3.4 Crystallinity

It is reasonable to study crystalline nature of solid sample through using XRD. At first, all samples show no significant diffractions on low-angle XRD (Fig. S4a–f, Sect. 4, supplementary material), indicating that these samples do not contain macroscopic symmetry. Secondly, powdered C1 shows two diffraction systems on wide-angle XRD. The first one could be assigned to cerianite, whose 2θ values are 28.54° (111), 33.08° (200), 47.48° (220), 56.34° (311), 59.08° (222), 69.41° (400), 76.70° (331), and 79.07° (420) (CeO_2 , PDF No. 34-0394; gray cubes in both Fig. 5a and Figs. S5a, S6a, Sects. 5, 6, supplementary material). Another one appears to be hydroxylbastnasite, with 2θ values at 17.72° (002), 24.59° (300), 30.47° (302), 35.89° (004), 43.28° (330), 43.99° (304), 50.41° (600), 53.86° (602), and 61.17° (306) (CeCO_3OH , PDF No. 52-0352; circles in both Fig. 5a and Figs. S5a, S6a). Alternatively, O 1s region of XPS of C1 may approve the presence of these two cerium components (Fig. S3a).

Next, in addition to the known phase of hydroxylbastnasite (CeCO_3OH , PDF No. 52-0352; circles in both C1 of Fig. 5 and Figs. S5a, S6b), there are still two systems on wide-angle XRD of C2. The first one seems to be cerium oxide carbonate hydrate ($\text{Ce}_2\text{O}(\text{CO}_3)_2\text{H}_2\text{O}$, PDF No. 43-0602; white cubes in both C2 of Fig. 5 and Figs. S5b, S6b), and the left one turns out to be cerium–yttrium mixed oxide ($\text{Y}_{0.50}\text{Ce}_{0.50}\text{O}_{1.75}$, PDF No. 75-0178; dots in both C2 of Fig. 5 and Figs. S5b, S6b). Based on comparison of wide-angle XRD of C2 and C1 (C1 and C2, Fig. 5), it appears that the binary metal oxide is formed during the present synthetic condition (C2 vs. C1, Scheme 1).

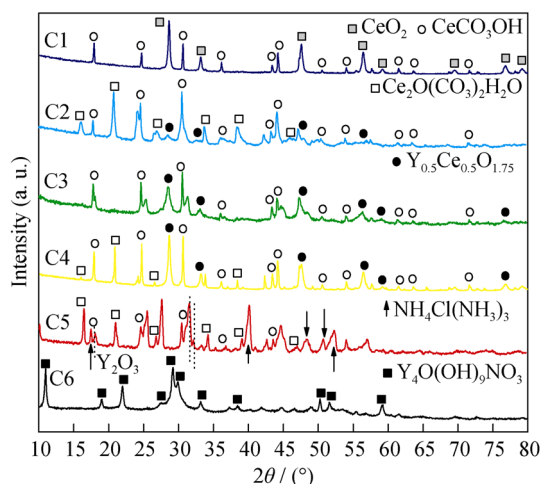


Fig. 5 Wide-angle XRD patterns of powdered C1, C2, C3, C4, C5, and C6

However, C2 contains more yttrium than cerium (Ce/Y item for C2, Table 1), and the residual yttrium may be accommodated in amorphous oxide.

When loading amounts of cerium and yttrium are the same under HMT in preparation (Scheme 1), the resulting C3 still contains hydroxylbastnasite (circles in both C3 of Fig. 5 and Figs. S5c, S6c) and cerium–yttrium mixed oxide (dots in both C3 of Fig. 5 and Figs. S5c, S6c), but original phase of cerium oxide carbonate hydrate on C2 disappears (C2 and C3, Fig. 5), probably because cerium content of solid sample is sharply decreased (C3 vs. C2 in Ce item, Table 1), when loading amount of yttrium is improved (C3 vs. C2, Scheme 1).

But interestingly, the wide-XRD pattern of C4 is changed back to that of C2 more than C3 (C2–C4, Fig. 5), where the phase of cerium oxide carbonate hydrate comes back ($\text{Ce}_2\text{O}(\text{CO}_3)_2\text{H}_2\text{O}$, PDF No. 43-0602; white cubes in both C4 of Fig. 5 and Figs. S5d, S6d). Herein, the use of HMT as additive in preparation reverses molar ratio of Ce/Y on solid product (C4 vs. C3, in Scheme 1 and Ce/Y item of Table 1), leaving excessive cerium, which gives cerium oxide carbonate hydrate with good crystallinity.

Then, when loading amount of yttrium exceeds that of cerium in preparation, the resulting C5 shows a little more complex wide-XRD than C3. In addition to the known phases of cerium oxide carbonate hydrate ($\text{Ce}_2\text{O}(\text{CO}_3)_2\text{H}_2\text{O}$, PDF No. 43-0602; white cubes in both C5 of Fig. 5 and Figs. S5e, S6e) as well as hydroxylbastnasite (CeCO_3OH , PDF No. 52-0352; circles in both C5 of Fig. 5 and Figs. S5e, S6e), there are another two phases on wide-XRD of C5, such as yttrium oxide (Y_2O_3 , PDF No. 44-0399; dot lines in both C5 of Fig. 5 and Figs. S5e, S6e), and ammonium chloride ammonia ($\text{NH}_4\text{Cl}(\text{NH}_3)_3$, PDF No. 73-1565; arrows both C5 of Fig. 5 and Figs. S5e, S6e). Herein, C5 shows a Ce/Y molar ratio of 1/33.5, which is much lower than 1/11 of C3 (Table 1), proposing that yttrium is excessive, which may appear as yttrium oxide has detectable crystallinity.

Lastly, C6 shows only one diffraction system on wide-angle XRD, which could be attributed to tetrayttrium oxide nonahydroxide nitrate, whose 2θ values are 11.02° (110), 18.88° (130), 21.68° (040), 27.33° (021), 29.09° (300), 29.97° (031), 32.78° (060), 38.55° (231), and 50.32° (–102) ($\text{Y}_4\text{O}(\text{OH})_9\text{NO}_3$, PDF No. 79-1352; dark cubes in both C6 of Fig. 5 and Figs. S5f, S6f), indicating that the present synthetic condition provides a hydroxynitric oxide rather than a pure yttrium oxide (C6, Scheme 1).

3.5 Textural property

Nitrogen physisorption provides a powerful method to study porosity of synthetic sample. First of all, C1 shows a Type III isotherm without hysteresis loop, along with a

pore size distribution whose highest point arrives at 1.0 nm (Fig. 6a) [36]. In association with morphology (Fig. 1a, b) and BET surface area (C1, Table 2, [37, 38]), C1 looks like a non-porous material [36]. When yttrium is doped into CeO₂ matrix (Scheme 1), the resulting C2 not only provides a Type H3 hysteresis loop (Fig. 6b) [36], along with a wide pore size distribution with the highest point at 1.1 nm (inset in Fig. 6b), but also exhibits a much higher BET surface area than C1 (Table 2), indicating C2 contains a lot of silt-shaped pores [36], which might be supported by the morphology of C2 obtained through SEM (Fig. 1c, d).

As efficiency of yttrium incorporation is increased continuously (C3 vs. C2, Table 1), the resulting C3 shows higher BET surface area and pore volume, as well as lower bulk density than C2 (Table 2), supposing that yttrium oxide is probably more porous than CeO₂, and meanwhile sample compositions have certain similarities (C2 and C3, Fig. 5). However, C5 contains more yttrium than C3 (Y and Ce/Y items, Table 2), chemical compositions of C5 and C3 become more different (C3 and C5, Fig. 5), giving poorer porosity to C5 (C5 vs. C3, Table 2). Obviously, there should be a phase transition, when loading of yttrium reaches a certain level in preparation (C5 vs. C3 vs. C2, in Scheme 1 and Table 2).

On the other hand, C3 shows higher BET surface area and pore volume, together with lower bulk density than C4 (Table 2), indicating that the presence of HMT in preparation not only improves yttrium incorporation on solid

product (C3 vs. C4, in Scheme 1 and Table 1), but also plays as pore-forming agent in synthesis. Additionally, C6 shows a Type IV isotherm along with Type H3 loop (Fig. 6f), whose pore size distribution is broad and centered at 5.8 nm (inset in Fig. 6f), characterizing a mesoporous material with silt-like mesopores [36], corresponding well to a new phase of tetrayttrium oxide nonahydroxide nitrate that is on wide-angle XRD (C6, Fig. 5).

With XRD and textural data obtained so far, it is significant to discuss particle sizes of synthetic sample stemming from different sources. Above all, the particle size of C1 originated from BET surface area is about six times as large as that from SEM (d_s of C1, Table 2 vs. Figure 1a, b), while that from SEM appears to be four times as broad as that from XRD (Fig. 1a, b vs. d_{XRD} of C1, Table 2). Herein, the size of BET surface area (d_s , Table 2) should represent scale of the smallest non-porous unit of C1, and meanwhile C1 is proved to be a non-porous material ($7 \text{ m}^2 \cdot \text{g}^{-1}$, Table 1), so it appears that six or seven particles (Fig. 1a, b) make up one non-porous unit during nitrogen physisorption experiment. Furthermore, the size stemming from XRD describes bulk phase of CeO₂ on C1, while the other part of C1 consists of other cerium components and organic species.

Based on above analysis, the comparisons of various particle sizes for other samples including C2–C6 become accessible (Fig. 1 and Table 2). In particular, there are basically uniform microflowers on SEM images of C5,

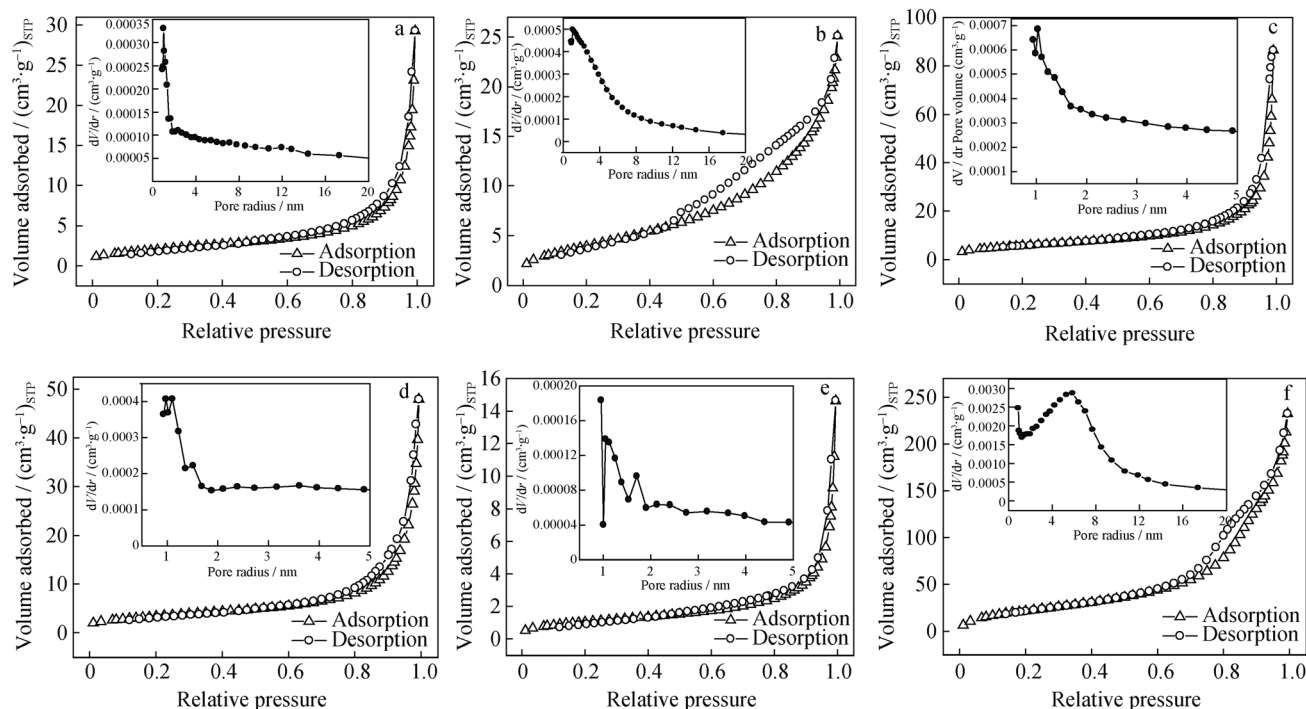


Fig. 6 Nitrogen adsorption–desorption isotherms and pore size distributions of **a** C1, **b** C2, **c** C3, **d** C4, **e** C5, and **f** C6 samples (STP: standard status)

Table 2 Textural properties of synthetic samples

Samples	$S_{\text{BET}}/(\text{m}^2 \cdot \text{g}^{-1})^{\text{a}}$	$\text{PV}/(\text{cm}^3 \cdot \text{g}^{-1})^{\text{b}}$	$\text{PV}_{\text{micro}}/(\text{cm}^3 \cdot \text{g}^{-1})^{\text{c}}$	$\text{PR}/\text{nm}^{\text{d}}$	$\rho/(\text{g} \cdot \text{cm}^{-3})^{\text{e}}$	$d_{\text{s}}/\text{nm}^{\text{f}}$	$d_{\text{XRD}}/\text{nm}^{\text{g}}$	Acid amount/ $(\text{mmol} \cdot \text{g}^{-1})^{\text{h}}$
C1	7	4.5×10^{-2}	0	10.9	1.3	659	24	1.24
C2	14	3.9×10^{-2}	0	4.4	1.2	357	15	0.65
C3	20	1.3×10^{-1}	0	11.8	1.1	272	11	0.97
C4	12	7.4×10^{-2}	0	11.3	1.2	416	20	1.02
C5	3	2.2×10^{-2}	0	11.4	1.3	1538	31	0.63
C6	84	3.6×10^{-1}	0	6.2	1.6	44	25	1.68

^aSurface area determined by BET method based on N_2 adsorption

^bPore volume, BJH adsorption cumulative volume of pores with radius of 0.85–150.00 nm

^c t -plot micropore volume

^dPore radius, BJH method on N_2 adsorption

^eBulk density

^fCrystallite size based on BET surface area: $d_{\text{s}} = 6/(S_{\text{BET}} \cdot \rho)$, ρ bulk density [37]

^gParticle diameter originated from XRD according to Scherrer's equation [38]: using 111 diffraction of CeO_2 for C1 (Fig. S5a), 111 of $\text{Y}_{0.5}\text{Ce}_{0.5}\text{O}_{1.75}$ for C2, C3 and C4 (b–d, Fig. S5), 200 of CeCO_3OH for C5 (Fig. S5e), and 110 of $\text{Y}_4\text{O}(\text{OH})_9\text{NO}_3$ (Fig. S5f)

^hDetermined by n-butylamine titration (Sect. 7 in Supplementary material)

where the scale of petals is ranged from 1.0 to 2.0 μm (Fig. 11–n). And meanwhile, the size coming from BET surface area of C5 is 1538 nm (Table 2). Therefore, the petals of C5 seem non-porous, and the microflower is composed of several non-porous petals (Fig. 11–n).

It is interesting to discuss the effect of preparative sol composition on acidity of sample. C6 shows a higher acid amount than C1 (Table 2), indicating the pure yttrium-containing sample has more acidic reactive centers than pure cerium-containing one. However, C1 shows a higher acid amount than all bimetallic samples including C2–C5 (Table 2), probably because doping yttrium to CeO_2 matrix provides various species (C1–C5, Fig. 5), exhibiting different distributions of acidic centers.

3.6 Functional group and thermal stability

It is significant to detect functional group of sample by using FTIR spectroscopy. First of all, C1 shows a small and a wide peak centering at 3735 and 3483 cm^{-1} (Fig. S7a, Sect. 8, supplementary material), probably corresponding to O–H stretching vibrations of hydroxyl groups coming from CeCO_3OH (C1, Fig. 5) and organic carboxyl residues (Fig. S2a), respectively. The sharp peak at 1644 cm^{-1} represents C=O stretching of carbonyl group (Fig. S7a), which has been approved by C 1s region of C1 (Fig. S2a).

Then, C1 also shows a peak with moderate intensity at 1445 cm^{-1} (Fig. S7a), probably approving asymmetric carbon–oxygen stretching of carboxyl group [39], while another small one at 1043 cm^{-1} may be ascribed to carbon–oxygen stretching of epoxy group (Fig. S7a) [40]. Lastly, C1 shows another three peaks at 676, 570 and

485 cm^{-1} , where the former one could be ascribed to Ce–O stretching vibration coming from CeCO_3OH , and the later two peaks both seem to be that from CeO_2 .

When yttrium begins to be loaded, the original peaks at 3735 and 3483 cm^{-1} on C1 are both degraded on C2 (Fig. S7a, b), reflecting that composition of solid sample is changed (C1 and C2, Fig. 5). C2 also shows two peaks with much higher intensities at 1500 and 1413 cm^{-1} (Fig. S7b), corresponding to carbon–carbon asymmetric stretching [41] and carbon–oxygen stretching of carboxyl group [40], respectively. Furthermore, the peaks at 844 and 722 cm^{-1} could be assigned to out-of-plane deformation and in-plane oscillation of methylene-containing alkyl chains [42]. Then, the small peaks appearing at 575 and 485 cm^{-1} may reflect the influences of both Ce–O and Y–O bonds.

Additionally, with the increase in loading amount of yttrium in preparation (Scheme 1), several other samples including C3–C5 show similar FTIR patterns as C2 (Fig. S7b–e), proposing their close structures in terms of functional group. However, C6 shows a more sophisticated FTIR spectrum than other samples, where the peaks at 3615 and 3511 cm^{-1} could be ascribed to O–H stretching vibrations of hydroxyl groups on $\text{Y}_4\text{O}(\text{OH})_9\text{NO}_3$ and organic species, respectively, while another one at 3398 cm^{-1} seems to be that on adsorbed water [43] (Fig. S7f).

The following two peaks that occurring at 2924 and 2867 cm^{-1} appear to be antisymmetric and symmetric stretching vibrations of C–H bond on methylene group (Fig. S7f) [43], probably stemming from organic residues of sample. There are still several peaks with lower

wavenumbers, which are basically similar to those found on FTIR of C2–C5 (Fig. S7b–f). Nevertheless, the peak at 1360 cm^{-1} could also be assigned to carbon–oxygen stretching of carboxyl group (Fig. S7f) [40].

Thermal analysis such as TGA and DSC would provide information on sample composition from another point of view. At the beginning, C1 shows a small weight loss of 1.3% at 30–150 °C (black line in Fig. 7), which could be ascribed to departure of adsorbed water or other volatile solvents under heating. However, this process does not involve significant heat effect at 30–300 °C, probably due to low content of volatiles, where the small sharp peak forming at 35–40 °C only represents instrumental noise (black line in Fig. S8, Sect. 9, Supplementary material).

As temperature rises, there is a large weight loss of 12.7% at 150–450 °C (black line in Fig. 7), indicating removal of organic components (Scheme 1). This process, however, does not mean a simultaneous endothermic effect below 300 °C (black line in Fig. S8), indicating some organic species are attached to metal-containing framework of C1 through physical adsorption more than chemical bond. C1 further shows a much smaller weight loss of 1.4% at 450–650 °C (black line in Fig. 7), which may be attributed to phase transition of metal components of C1 such as CeO_2 and CeCO_3OH (Fig. 5a).

Several other samples involving C2–C5 all show similar TGA and DSC patterns as C1 (Fig. 7 and Fig. S8), successively representing removals of adsorbed water, physically adsorbed organic species, chemically bonded organic species, along with phase transition of metal component. On the other hand, the weight loss processes below 300 °C have nothing to do with thermal effects at all (Fig. 7 and Fig. S8).

But in particular, C6 shows a different TGA curve than the former five samples. There are four weight losses at 30–800 °C. The first one staying at 30–150 °C accounts for 8.7% of total mass (brown line in Fig. 7), corresponding to a broad endothermic band at 50–150 °C (brown line in

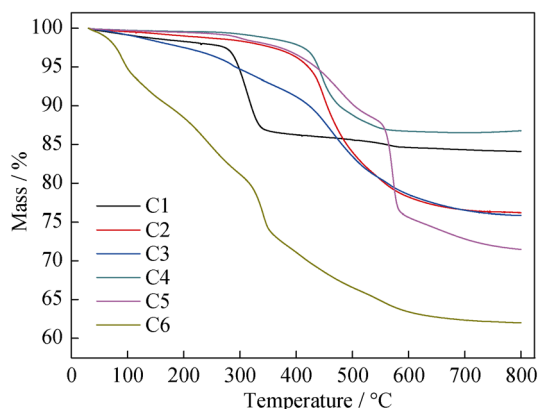


Fig. 7 TGA curves of synthetic samples

Fig. S8), proposing departure of adsorbed water or volatiles under heating. The following one of 8.4% occurs at 150–275 °C (brown line in Fig. 7), which is accompanied by another endothermic band at 175–300 °C (brown line in Fig. S8). Furthermore, C6 shows a sharp weight loss of 14.21% at 275–450 °C (brown line in Fig. 7). The second and third weight losses may suppose removal of organic species. C6 shows the last weight loss of 6.2% at 450–700 °C (brown line in Fig. 7), probably indicating the phase transition of metal component.

3.7 Monitoring of sample formation

It is significant to monitor sample formation through measurement of various parameters of preparative sol. At first, based on detection of aqueous particle size of C1 precursor (Fig. 8a), it can be seen that the micelle size is changed from big to small, then back to big again (Fig. 8a; circles in Fig. 8b), and meanwhile zeta potential is varied accordingly (triangles in Fig. 8b), indicating that formation of C1 precursor in sol–gel undergoes a process that varied from stable to unstable, then back to stable, mainly because a higher and balanced zeta potential is beneficial to stability of solvated particle [44].

Next, it seems interesting to study whether size variation of C1 precursor means alteration of chemical bond, so UV–Vis spectroscopy was measured. In practice, the adsorption of C1 precursor appearing at 297 nm continues to rise (black, blue, to other colors in Fig. 8c), which could be ascribed to charge transfer transition of organic species [45], obviously indicating that there are chemical reactions during formation and stabilization of C1 precursor.

Lastly, based on above observations, a formation mechanism of sample morphology is proposed in Fig. 9. First of all, it was reported previously that the self-assembly of PVP with silica precursor would produce silica nanoparticles, which are further agglomerated into porous silica microspheres [46]. Obviously, PVP may be also self-assembled into micelles in the present system, which are further agglomerated to larger colloids (Fig. 9). This procedure might proceed too fast to incorporate any metals. But as reaction continues, the colloids obtained so far would be merged with cerium component through chemical reaction, according to UV–Vis monitoring (297 nm in Fig. 8c), probably leading to ball composite, and the uniform cube-like nanoparticles of C1 would be formed and collected after aging of gel (Fig. 9).

On the other hand, formation of C4 shows a similar pattern as that of C1 (Fig. 8a, b, d, e), while the most significant difference is that UV–Vis adsorption of C4 shows very limited improvements at 297 nm (Fig. 8f). And meanwhile, the adsorption at 297 nm of C6 almost remains unchanged (Fig. 8i). Therefore, taking into account that C1

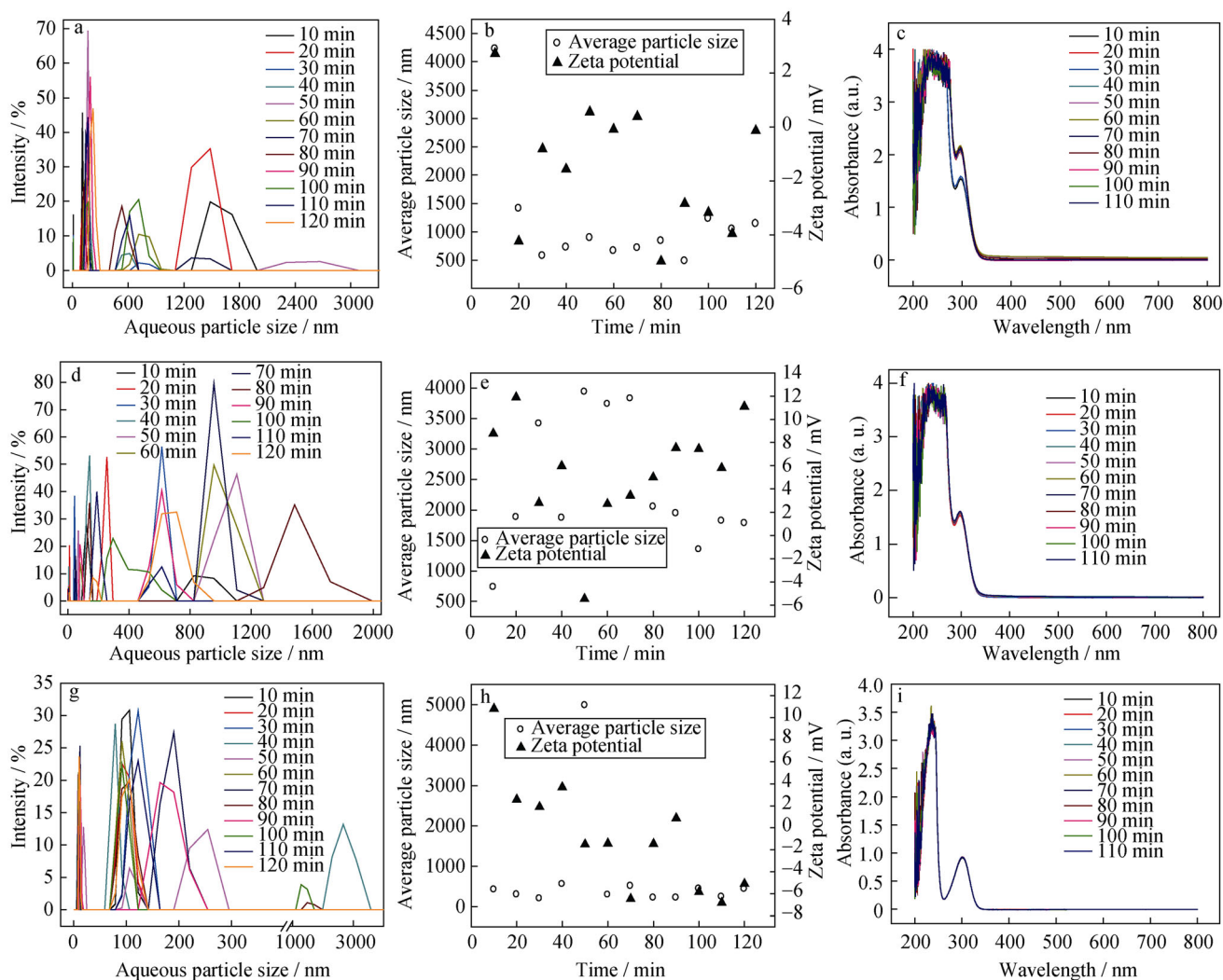


Fig. 8 Real-time monitoring of **a, d, g** aqueous particle size, **b, e, h** zeta potential and **c, f, i** UV-Vis spectroscopy for C1, C4, and C6 samples, accordingly

only contains cerium, C4 has both cerium and yttrium, and C6 only owns yttrium (Scheme 1, Table 1), it is cerium instead of yttrium that brings about chemical changes of PVP colloid during sample formation (Fig. 9). Furthermore, perhaps due to interaction of PVP colloid with various metal component (C1, C4, C6, Scheme 1), three kinds of solvated composite may be obtained (Fig. 9), leading to a variety of sample morphologies (Fig. 1a, b, i, j, k, o, p).

3.8 Catalytic dehydration property

First of all, it is necessary to test effect of solvent during catalysis. When dehydration was carried out at 20 °C, dichloromethane shows better conversion of aniline than water for both C1 (Entries 3 vs. 5 in Table 3) and C4 (Entries 9 vs. 11 in Table 3). Herein, aniline is probably

more soluble in dichloromethane than in water [47], which affects dispersion of substrate into catalytic center. Taking into account that C1 and C4 show different metal compositions (Table 1), this result might also indicate that both pure cerium and cerium–yttrium mixed components prefer dichloromethane to water during catalytic dispersion.

Next, discussion of temperature may provide information on energy conversion. In practice, a higher temperature (80 °C) shows better substrate conversions than a lower one (20 °C) for the reactions catalyzed by C4 and C6 (Entries 10 vs. 9, 15 vs. 14 in Table 3), but a conversed tendency is found for that by C5 (Entries 13 vs. in 12, Table 3). Herein, C5 has a different crystalline structure from C4 and C6 (Fig. 5d–f), particularly regarding $\text{NH}_4\text{Cl}(\text{NH}_3)_3$, an inorganic salt on C5 (Fig. 5e). In view of a poor BET surface area of C5 ($3 \text{ m}^2 \cdot \text{g}^{-1}$, Table 2), this

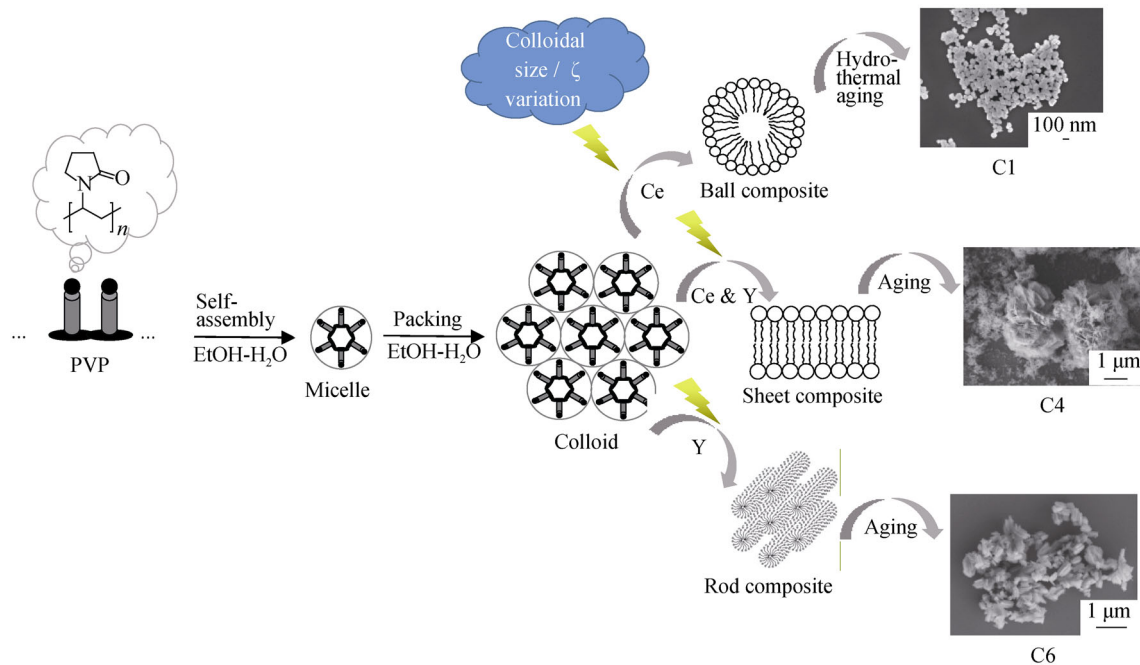
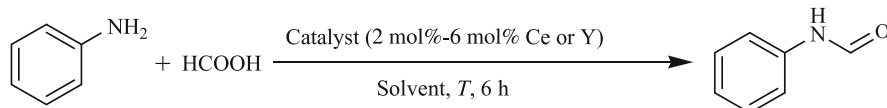


Fig. 9 Proposed process for sample formation

Table 3 Catalytic dehydration for preparation of N-phenylformamide

Entry ^a	Catalyst	Cat. loading/mol% ^a	Solvent	<i>T</i> /°C	Conversion/% ^b	Yield of amide/% ^c
1	Na ₂ SO ₄	10	CH ₂ Cl ₂	20	0	0
2	DCC/DMAP	2	CH ₂ Cl ₂	20	45	45
3	C1	2	CH ₂ Cl ₂	20	68	68
4	–	6	CH ₂ Cl ₂	20	66	66
5	–	2	H ₂ O	20	43	43
6	C2	2	CH ₂ Cl ₂	20	67	67
7	C3	2	CH ₂ Cl ₂	20	68	68
8	–	6	CH ₂ Cl ₂	20	37	37
9	C4	2	CH ₂ Cl ₂	20	58	58
10	–	2	CH ₂ Cl ₂	80	71	71
11	–	2	H ₂ O	20	38	38
12	C5	2	CH ₂ Cl ₂	20	70	70
13	–	2	CH ₂ Cl ₂	80	64	64
14	C6	2	CH ₂ Cl ₂	20	29	29
15	–	2	CH ₂ Cl ₂	80	69	69

Formula



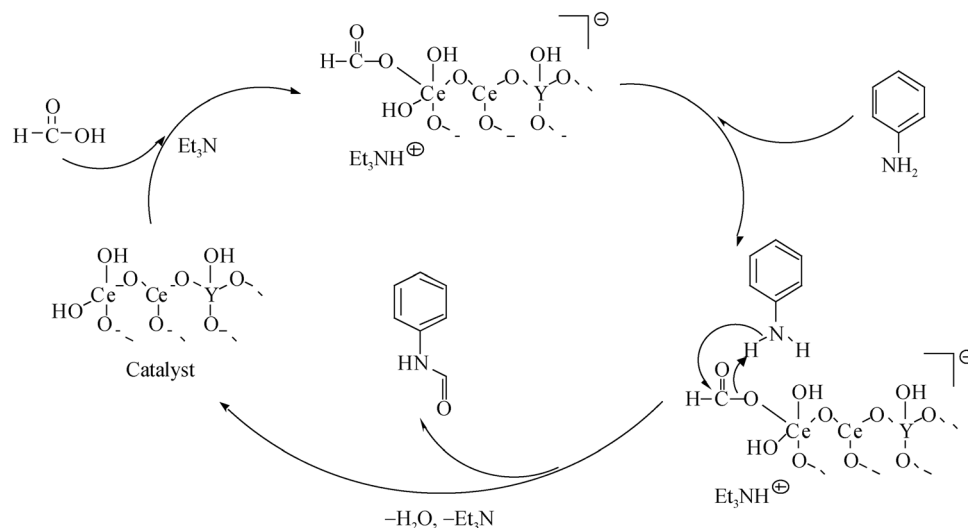
^aDetails as in Sect. 2.4, Cat. means catalyst

^bConversion of aniline to all possible dehydrated products, determined by GC–MS (Sect. 11 in Supplementary material)

^cYield of N-phenylformamide based on aniline, determined by GC–MS (Sect. 11 in Supplementary material)

salt may be activated under heating and then saturates metal centers, or blocks dispersion path of substrate onto active centers of C5.

Then, it is important to compare catalysts under various conditions. In general, all reactions proceed smoothly, where dehydrated compound is usually the only product,



Scheme 2 A proposed mechanism for catalytic amidation

and no by-products are detected (Table 3). When dehydration is performed in dichloromethane at 20 °C, anhydrous Na_2SO_4 could not give any products, while DCC/DMAP provides conversion of 45% (Entries 1, 2 in Table 3). In spite of C6, however, most synthetic catalysts including C1–C5 show higher substrate conversions than DCC/DMAP (Entries 3, 6, 7, 9, 12 vs. 2 in Table 3), approving the unique dehydration property of present system.

On the other hand, C1, C2, C3, and C5 show almost equal substrate conversions (Entries 3, 6, 7, 12 in Table 3), but performance of C4 seems less effective (Entry 9 in Table 3), and C6 shows the lowest output (Entry 14 in Table 3). Herein, the former five catalysts including C1–C5 all contain cerium components such as oxide and salt, but no cerium is found on C6 (Fig. 5a–f), leading to difference of activity.

Furthermore, preparations of C3 and C4 are almost identical except for the use of HMT as additive (Scheme 1), which gives different Ce/Y molar ratios on solid product (Table 1), also affecting catalytic output (Entries 7 vs. 9 in Table 3). Improving catalyst loading amount would not show higher substrate conversions for both C1 and C3 (Entries 4 vs. 3, 8 vs. 7 in Table 3), which probably means a higher catalyst content in solution may adsorb or fix substrates or products, leading to poorer conversion.

At last, it is also interesting to study kinetic aspect of this system. Based on UV–Vis monitoring of catalytic solution (Fig. S9a–c, Sect. 10, supplementary material), it can be seen that C1 shows the best conversion efficiency within the former fifty minutes (green columns in Fig. S9d), C4 the second (red), and C6 the last (blue). In association with the fact that C6 is much less efficient than

C1–C5 (Entries 14 vs. 3, 6, 7, 9, 12 in Table 3), cerium turns out to be catalytic center beyond yttrium. Alternatively, the present catalytic system provides an efficient and clean process for synthesis of N-phenylformamide, which is comparable to many known systems in respects of reaction complexity [20], catalyst cost [21], and benign and clean manipulation [48].

On the other hand, a mechanism of catalytic amidation is proposed in Scheme 2 on the basis of both characterization and catalytic results. Probably, the adsorption and activation of formic acid over cerium center of catalyst may trigger the catalytic cascade [25], and the subsequent nucleophilic attack of aniline would accomplish this transformation (Scheme 2). Herein, yttrium of catalyst may play as structural component more than catalytic center (Scheme 2).

4 Conclusion

A series of cerium–yttrium mixed oxides were prepared by using polyvinylpyrrolidone as structure-directing agent through a sol–gel process. Characterizations reveal that composition of preparative solution plays a key role in determination of sample morphology, while use of hexamethylenetetramine as additive could reverse metal ratio of solid product. Then, based on the monitoring of aqueous particle size, zeta potential, and UV–Vis during formation of sol, it is proposed that self-assembly of polyvinylpyrrolidone and its subsequent reaction with metal ion would determine final sample morphology.

In catalytic amidation, all synthetic catalysts show high conversions, which are comparable to those derived from anhydrous Na_2SO_4 and DCC/DMAP combination, showing

prospects for large-scale application. The dichloromethane shows better outputs than water, but increasing catalyst loading could not improve conversion. Introduction of hexamethylenetetramine to catalyst improves activity, cerium looks more active than yttrium for catalytic amidation, while yttrium mainly plays as an both structure-directing and pore-forming agent. In general, this work not only provides an interesting and significant series of cerium–yttrium binary oxides with particular morphologies, but also shows their attractive application for catalytic amidation, which means a lot to deep utilization of rare metals as well as efficient and eco-friendly organic processes.

Acknowledgements This study was financially supported by the Natural Science Foundation of Shaanxi Province (No. 2017JM2016), and the Fundamental Research Funds for the Central Universities (No. xjj2014005).

References

- [1] Zhang G, Xu J, Hou Z, Wang Q. Research on micro-structure and catalysis properties of nanosized $Ce_{1-x}(Fe_{0.5}Eu_{0.5})_xO_{2-\delta}$ solid solutions. *J Rare Earths*. 2017;35(1):63.
- [2] Shen K, Lin J-P, Xia Q, Dai L, Zhou G-J, Guo Y-L, Lu G-Z, Zhan W-C. Tuning performance of $Pd/Sn_{0.9}Ce_{0.1}O_2$ catalyst for methane combustion by optimizing calcination temperature of support. *Rare Met*. 2019;38(2):107.
- [3] Minaei S, Haghghi M, Jodeiri N, Ajamein H, Abdollahifar M. Urea-nitrates combustion preparation of CeO_2 -promoted $CuO/ZnO/Al_2O_3$ nanocatalyst for fuel cell grade hydrogen production via methane steam reforming. *Adv Powder Technol*. 2017;28(3):842.
- [4] Sun C, Li H, Chen L. Nanostructured ceria-based materials: synthesis, properties, and applications. *Energy Environ Sci*. 2012;5(9):8475.
- [5] Han X, Li L, Wang C. Template-free synthesis of uniform single-crystal hollow cerium dioxide nanocubes and their catalytic activity. *Nanoscale*. 2013;5(16):7193.
- [6] Yuan S, Zhang Q, Xu B, Jin Z, Zhang Y, Yang Y, Zhang M, Ohno T. Porous cerium dioxide hollow spheres and their photocatalytic performance. *RSC Adv*. 2014;4(107):62255.
- [7] Slavinskaya EM, Kardash TY, Stonkus OA, Gulyaev RV, Lapin IN, Svetlichnyi VA, Boronin AI. Metal-support interaction in Pd/CeO_2 model catalyst for CO oxidation: from pulsed laser-ablated nanoparticles to highly active state of the catalyst. *Catal Sci Technol*. 2016;6(17):6650.
- [8] Wilklow-Marnell M, Jones WD. Catalytic oxidation of carbon monoxide by α -alumina supported 3 nm cerium dioxide nanoparticles. *Mol Catal*. 2017;9:439.
- [9] Channei D, Nakaruk A, Phanichphant S. Influence of graphene oxide on photocatalytic enhancement of cerium dioxide. *Mater Lett*. 2017;209:43.
- [10] Satapathy S, Ahlawat A, Paliwal A, Singh R, Singh MK, Gupta PK. Effect of calcination temperature on nanoparticle morphology and its consequence on optical properties of $Nd:Y_2O_3$ transparent ceramics. *CrystEngComm*. 2014;16(13):2723.
- [11] Hayashi F, Iwamoto M. Yttrium-modified ceria as a highly durable catalyst for the selective conversion of ethanol to propene and ethene. *ACS Catal*. 2013;3(1):14.
- [12] Fokema MD, Ying JY. The selective catalytic reduction of nitric oxide with methane over scandium oxide, yttrium oxide and lanthanum oxide. *Appl Catal B: Environ*. 1998;18(1–2):71.
- [13] Park J, Park M, Nam G, Kim MG, Cho J. Unveiling the catalytic origin of nanocrystalline yttrium ruthenate pyrochlore as a bifunctional electrocatalyst for Zn-air batteries. *Nano Lett*. 2017;17(6):3974.
- [14] Cheng W, Rechberger F, Niederberger M. Three-dimensional assembly of yttrium oxide nanosheets into luminescent aerogel monoliths with outstanding adsorption properties. *ACS Nano*. 2016;10(2):2467.
- [15] Englade-Franklin LE, Morrison G, Verberne-Sutton SD, Francis AL, Chan JY, Garno JC. Surface-directed synthesis of erbium-doped yttrium oxide nanoparticles within organosilane zeptoliter containers. *ACS Appl Mater Interfaces*. 2014;6(18):15942.
- [16] Olad A, Zebhi H, Salari D, Mirmohseni A, Reyhanitabar A. Synthesis, characterization, and swelling kinetic study of porous superabsorbent hydrogel nanocomposite based on sulfonated carboxymethylcellulose and silica nanoparticles. *J Porous Mater*. 2018;25(5):1325.
- [17] Taha AKT, Amir M, Korkmaz AD, Al-Messiere MA, Baykal A, Karakuş S, Kilislioglu A. Development of novel nano-ZnO enhanced polymeric membranes for water purification. *J Inorg Organomet Polym*. 2019;29(3):979.
- [18] Yan N, Zhang J, Tong Y, Yao S, Xiao C, Li Z, Kou Y. Solubility adjustable nanoparticles stabilized by a novel PVP based family: synthesis, characterization and catalytic properties. *Chem Commun*. 2009;29:4423.
- [19] Zaki T. Catalytic dehydration of ethanol using transition metal oxide catalysts. *J Colloid Interf Sci*. 2005;284(2):606.
- [20] Hu L, Xu S, Zhao Z, Yang Y, Peng Z, Yang M, Wang C, Zhao J. Ynamides as racemization-free coupling reagents for amide and peptide synthesis. *J Am Chem Soc*. 2016;138(40):13135.
- [21] Mai TT, Viswambharan B, Gori D, Kouklovsky C, Alezra V. Memory of chirality of tertiary aromatic amide: application to the asymmetric synthesis of (*S*)- α -methylDOPA. *J Org Chem*. 2012;77(19):8797.
- [22] Ojeda-Porras A, Gamba-Sánchez D. Recent developments in amide synthesis using nonactivated starting materials. *J Org Chem*. 2016;81(23):11548.
- [23] Dunetz JR, Magano J, Weisenburger GA. Large-scale applications of amide coupling reagents for the synthesis of pharmaceuticals. *Org Process Res Dev*. 2016;20(2):140.
- [24] Dine TME, Erb W, Berhault Y, Rouden J, Blanchet J. Catalytic chemical amide synthesis at room temperature: one more step toward peptide synthesis. *J Org Chem*. 2015;80(9):4532.
- [25] Potadar SM, Mali AS, Waghmode KT, Chaturbhuj GU. Repurposing *n*-butyl stannic acid as highly efficient catalyst for direct amidation of carboxylic acids with amines. *Tetrahedron Lett*. 2018;59(52):4582.
- [26] Renuka MK, Gayathri V. Synthesis of secondary amides by direct amidation using polymer supported copper(II) complex. *Polyhedron*. 2018;148:195.
- [27] Kang B, Fu Z, Hong SH. Ruthenium-catalyzed redox-neutral and single-step amide synthesis from alcohol and nitrile with complete atom economy. *J Am Chem Soc*. 2013;135(32):11704.
- [28] Mía S, Dijkstra FA, Singh B. Aging induced changes in biochar's functionality and adsorption behavior for phosphate and ammonium. *Environ Sci Technol*. 2017;51(15):8359.
- [29] Chen D, He D, Lu J, Zhong L, Liu F, Liu J, Yu J, Wan G, He S, Luo Y. Investigation of the role of surface lattice oxygen and bulk lattice oxygen migration of cerium-based oxygen carriers: XPS and designed H_2 -TPR characterization. *Appl Catal B: Environ*. 2017;218:249.

- [30] Pawlak DA, Woźniak K, Frukacz Z, Barr TL, Fiorentino D, Hardcastle S. ESCA studies of yttrium orthoaluminum perovskites. *J Phys Chem B*. 1999;103(17):3332.
- [31] Pawlak DA, Woźniak K, Frukacz Z, Barr TL, Fiorentino D, Seal S. ESCA studies of yttrium aluminum garnets. *J Phys Chem B*. 1999;103(9):1454.
- [32] Galindo IR, Viveros T, Chadwick D. Synthesis and characterization of titania-based ternary and binary mixed oxides prepared by the sol-gel method and their activity in 2-propanol dehydration. *Ind Eng Chem Res*. 2007;46(4):1138.
- [33] Lee AF, Naughton JN, Liu Z, Wilson K. High-pressure XPS of crotyl alcohol selective oxidation over metallic and oxidized Pd(111). *ACS Catal*. 2012;2(11):2235.
- [34] Zhang Y, Yuwono AH, Wang J, Li J. Enhanced photocatalysis by doping cerium into mesoporous titania thin films. *J Phys Chem C*. 2009;113(51):21406.
- [35] Imamura M, Matsubayashi N, Shimada H. Catalytically active oxygen species in $\text{La}_{1-x}\text{Sr}_x\text{CoO}_{3-\delta}$ studied by XPS and XAFS spectroscopy. *J Phys Chem B*. 2000;104(31):7348.
- [36] Sing KSW, Everett DH, Haul RAW, Moscou L, Pierotti RA, Rouquérol J, Siemieniewska T. Reporting physisorption data for gas/solid systems with special reference to the determination of surface area and porosity. *Pure Appl Chem*. 1985;57(4):603.
- [37] Hiyoshi N. Nanocrystalline sodalite: preparation and application to epoxidation of 2-cyclohexen-1-one with hydrogen peroxide. *Appl Catal A: Gen*. 2012;419–420:164.
- [38] Zhan H, Yang X, Wang C, Chen J, Wen Y, Liang C, Greer HF, Wu M, Zhou W. Multiple nucleation and crystal growth of barium titanate. *Cryst Growth Des*. 2012;12(3):1247.
- [39] Vinothkannan M, Kim AR, Nahm KS, Yoo DJ. Ternary hybrid (SPEEK/SPVdF-HFP/GO) based membrane electrolyte for the applications of fuel cells: profile of improved mechanical strength, thermal stability and proton conductivity. *RSC Adv*. 2016;6(110):108851.
- [40] Rodríguez-González C, Martínez-Hernández AL, Castaño VM, Kharissova OV, Ruoff RS, Velasco-Santos C. Polysaccharide nanocomposites reinforced with graphene oxide and keratin-grafted graphene oxide. *Ind Eng Chem Res*. 2012;51(9):3619.
- [41] Ramaprasad AT, Latha D, Rao V. Synthesis and characterization of polypyrrole grafted chitin. *J Phys Chem Solids*. 2017;104:169.
- [42] Barroso-Bogeat A, Alexandre-Franco M, Fernández-González C, Gómez-Serrano V. FT-IR analysis of pyrone and chromene structures in activated carbon. *Energy Fuels*. 2014;28(6):4096.
- [43] Zhang H, Wang YM, Zhang L, Gerritsen G, Abbenhuis HCL, van Santen RA, Li C. Enantioselective epoxidation of β -methylstyrene catalyzed by immobilized Mn(salen) catalysts in different mesoporous silica supports. *J Catal*. 2008;256(1):226.
- [44] Huo W, Zhang X, Gan K, Chen Y, Xu J, Yang J. Effect of zeta potential on properties of foamed colloidal suspension. *J Eur Ceram Soc*. 2019;39(2–3):574.
- [45] Cheng H, Qin L, Cai P, Chen C, Wang J, Kim SI, Huang Y, Seo HJ. Charge transfer transition and energy transfer in Eu^{3+} -doped $\text{Gd}_{10}\text{V}_2\text{O}_{20}$. *J Lumin*. 2018;195:278.
- [46] Park J, Cullen DA, Chen J, Polizo G, Sharma J. Same solution synthesis and self-assembly of porous silica nanoparticles into microspheres. *Appl Surf Sci*. 2019;467–468:634.
- [47] Santos SI, Bogel-Lukasik E, Bogel-Lukasik R. The ionic liquid effect on solubility of aniline, a simple aromatic amine: perspective of solvents' mixture. *Fluid Phase Equilib*. 2012;325:105.
- [48] Chen C, Tan L, Zhou P. Approach for the synthesis of N-phenylamides from β -ketobutylanilides using dimethylformamide and dimethylacetamide as the acyl donors. *J Saudi Chem Soc*. 2015;19(3):327.